

L-band ($3.5 \mu\text{m}$) IR-excess in massive star formation

II. RCW 57/NGC 3576[★]

M. Maercker,^{1,2} M. G. Burton² and C. M. Wright³

¹ Stockholm Observatory, AlbaNova University Center,
106 91 Stockholm, Sweden
e-mail: maercker@astro.su.se

² School of Physics, University of New South Wales,
Sydney, NSW 2052, Australia
e-mail: mgb@phys.unsw.edu.au

³ School of Physical, Environmental and Mathematical Sciences, University of New South Wales@ADFA
Canberra, ACT 2600, Australia
e-mail: c.wright@adfa.edu.au

Received October 18, 2005; accepted December 7, 2005

Abstract. We present a JHK_sL survey of the massive star forming region RCW 57 (NGC 3576) based on L-band data at $3.5 \mu\text{m}$ taken with SPIREX (South Pole Infrared Explorer), and 2MASS JHK_s data at $1.25\text{--}2.2 \mu\text{m}$. This is the second of two papers, the first one concerning a similar JHK_sL survey of 30 Doradus. Colour-colour and colour-magnitude diagrams are used to detect sources with infrared excess. This excess emission is interpreted as coming from circumstellar disks, and hence gives the cluster disk fraction (CDF). Based on the CDF and the age of RCW 57, it is possible to draw conclusions on the formation and early evolution of massive stars. The infrared excess is detected by comparing the locations of sources in JHK_sL colour-colour and L vs. (K_s-L) colour-magnitude diagrams to the reddening band due to interstellar extinction. A total of 251 sources were detected. More than 50% of the 209 sources included in the diagrams have an infrared excess. Comparison with other JHK_sL surveys, including the results on 30 Doradus from the first paper, support a very high initial disk fraction (>80%) even for massive stars, although there is an indication of a possible faster evolution of circumstellar disks around high mass stars. 33 sources only found in the L-band indicate the presence of heavily embedded, massive Class I protostars. We also report the detection of diffuse PAHs emission throughout the RCW 57 region.

Key words. Stars: circumstellar matter, formation, evolution, Hertzsprung-Russel (HR) and C-M diagrams, protoplanetary disks, pre-main sequence

1. Introduction

1.1. IR-excess as a measure of circumstellar disks

This paper is the second of two papers using IR-excess in the JHK_sL plane ($1.2 - 3.5 \mu\text{m}$) to measure the fraction of sources with circumstellar disks in high mass star forming regions. The first paper concerned 30 Doradus in the LMC (Maercker & Burton (2005), from now referred to as Paper I). IR-excess can be detected using near infrared colour-colour diagrams by comparing the position of sources relative to the reddening vectors due to interstellar extinction. The excess radiation above that of a blackbody can be explained by models of circumstellar disks around a young stellar object (eg. Lada & Adams (1992)). Although this excess radiation can be detected using

JHK_s data ($1.2 - 2.2 \mu\text{m}$) alone, the nature of IR-excess is not always clear. JHK_sL observations give a larger separation to the IR-excess sources in colour-colour diagrams, whereas JHK_s observations tend to underestimate the fraction of stars with IR-excess. On account of the difficulties of ground based observations at longer wavelengths, the L-band ($3.5 \mu\text{m}$) proves to be the best wavelength for detecting circumstellar disks, although longer wavelengths are preferable, if space observations are available. Kenyon & Hartmann ((1995)) show the advantage of (K_s-L) as a measure of IR-excess by comparing the frequency distributions in young stellar clusters for (H-K_s) and (K_s-L). Whereas the (H-K_s) distribution has one clear peak at (H-K_s) $\sim 0.2\text{--}0.4$ and a long tail, the (K_s-L) distribution has a clear second peak at (K_s-L) $\sim 0.8\text{--}1.0$ made up mostly of class II sources with optically thick, circumstellar disks.

[★] Table 7 is only available in electronic form at the CDS via anonymous ftp to cdsarc.u-strasbg.fr (130.79.128.5) or via <http://cdsweb.u-strasbg.fr/cgi-bin/qcat?J/A+A/>

1.2. RCW 57

This young massive star forming region, also known as NGC 3576, is one of the brightest HII regions in the infrared in our Galaxy. The kinematic distance is 3.0 ± 0.3 kpc, adopted from De Pree et al. ((1999)). An asymmetrical structure in the region can be seen in the 21 cm map by Retallack & Goss ((1980)), which extends to the northeast but has a sharp cut off in the southwest. The spectral energy distributions of five objects detected using a 10 μm map (Frogel & Persson (1974)) suggest that these are protostellar objects with silicate absorption features, therefore indicating Class I objects (Persi et al. (1994)). Near infrared photometry by Persi et al., together with an 8 - 13 μm CVF spectrum of IRS 1 (IRAS 11097-6102 in the IRAS Point Source Catalogue), show that the majority of stars (> 70%) have an infrared excess in the JHK_s plane. 19 of these sources could be matched with the present data, 15 of which we show can also be classified as having an infrared excess in the JHK_sL plane. The sources discussed by Persi et al. are confined to the central region, confirming the youth of the cluster. Radio recombination lines were detected by McGee & Gardner ((1968)), Wilson et al. ((1970)) and De Pree et al. ((1999)). The detection of maser sources in CH₃OH and H₂O (Caswell et al. (1995) and (1989) respectively) are indications of early stages of star formation in a dense circumstellar environment. Thorough investigations of the central region have been undertaken by Figuerêdo et al. ((2002)) in the near-infrared (NIR), and Barbosa et al. ((2003)) in the mid-infrared (MIR). Nine of the MIR sources match sources seen in the L-band image presented here. In the NIR, JHK_s colour-colour and colour-magnitude diagrams show sources affected by excess emission, indicating the presence of circumstellar disks around the less massive members of the cluster (Figuerêdo et al. (2002)). Eight spectra of the brightest sources show rising continua towards the IR. Three of these have a clear infrared excess. The detection of CO bandheads (2.2935 μm) in emission and absorption indicates the presence of several sources still heavily embedded in their stellar birthclouds (Figuerêdo et al. (2002), Barbosa et al. (2003)). Based on the radio data (Goss & Shaver (1970)), RCW 57 can be classified as a Giant HII (GHII) region, with 1.6×10^{50} photons s⁻¹ in the UV (defining sources brighter than 10^{50} Lyman continuum photons per second as GHII regions (Figuerêdo et al. (2002))). A possible ionizing source has been found at the peak emission of the 3.4 cm map (DePree et al. (1999)), the source being a cluster of stars that have broken out of their natal cocoons but remain hidden behind dark clouds along the line of sight (Barbosa et al. (2003)). The radio peak emission (at \sim RA 11h11m51s, Dec -61°18'45''(J2000)) is also hidden behind clouds in the SPIREX image. This is further confirmed by Walsh et al ((2001)), who find the peak of the 8.64 GHz continuum emission to lie at approximately the same position, behind clouds in the N-band image (their Fig. 2). In their follow up survey, Barbosa et al. for the first time resolved IRS 1 into four sources in the 10 μm band, approximately 1.5'' apart from each other (Nos. 48, 50, 60 and 60b in their paper. Source numbers labelled in Table 7 with 'No' and a number are from Barbosa et al.). One of these shows evidence for a UC HII region and they conclude that the sources in the

central region of RCW 57 are in the UC HII region phase. The position of IRS 1 coincides with the brightest L-band source in our study ($m_L=4.1$, #88, Table 7) and is also found in the L-band by Moneti ((1992)) with magnitude $m_L=4.05$. Barbosa et al. also found a new MIR source, without a counterpart in the NIR, which is possibly a hot core. In the central region a strong CO $J = 2 - 1$ line at 230 GHz was observed by White and Phillips ((1983)). Shock-excited H₂ line emission may also indicate the presence of gas outflows (Figuerêdo et al. (2002)).

2. Observations

2.1. L-band data from SPIREX

The data at 3.5 μm was taken with the 60 cm South Pole InfraRed Explorer (SPIREX) (Hereld (1994); Burton et al. (2000)) at the Amundsen-Scott South-Pole Station using the Abu camera equipped with a 1024x1024 InSb array (Fowler et al. (1998)) in July and August 1999. Observations were carried out using the L-band filter ($\lambda_{\text{central}}=3.514$ μm , $\Delta\lambda=0.618$ μm) and had a field of view of 10' and pixel scale 0.6''. The image is a mosaic of a series of 3 minute frames, each shifted by 15'' from each other, interleaved with separate sky observations, and comprises a total of 60 minutes of on-source integration. Reductions were done automatically using the SPIREX/Abu pipeline¹. Unfortunately the data was not flux calibrated and separate observations were necessary to determine the calibration, as discussed in Paper I (see § 2.4).

2.2. Narrow Band Filters from SPIREX

In addition to the L-band data, images were obtained through three narrow band filters, centred on the wavelengths of the H₂ v=1-0 Q-branch lines, a PAHs emission feature, and the hydrogen Br α line. The line centres of the filters were 2.42, 3.30 and 4.05 μm , respectively, and their widths 0.034, 0.074 and 0.054 μm . For the H₂ and PAHs filters the data were self-calibrated using interpolated values for magnitudes of the sources IRS1, Persi 43 and Persi 106 (stars 88, 74 and 124, respectively in Table 7) from those we determined in this Table for the K_s and L bands. For the Br α filter, we self-calibrated based on a flux for IRS1 of 16 Jy at 4 μm , as measured by McGregor et al. ((1984)).

2.3. JHK_s-band data from 2MASS

The L-band observations were complemented with JHK_s data from the 2MASS point source catalogue (PSC) (Cutri et al. (2003)) and atlas images². The 2MASS telescopes (Kleinmann et al. (1994)) scanned the sky in both hemispheres in three near infrared filters (J, H and K_s; 1.25, 1.65 and 2.2 μm respectively) with limiting magnitudes of $m_J=15.8$, $m_H=15.1$ and $m_K=14.3$. The L-band data was first matched with sources in the PSC. Photometry was also performed on the K_s-band atlas images to derive the magnitudes for any sources that could not be matched with those in the PSC.

¹ <http://pipe.cis.rit.edu>

² Available at <http://www.ipac.caltech.edu/applications/2MASS/IM/>

Table 1. Standard star used to calibrate the CASPIR images (McGregor (1994)).

name	RA (J2000) (h m s)	DEC(J2000) (d m s)	m_L Mag
BS4638	12 11 39.1	-52 22 06	4.501

Table 2. Stars in RCW 57 used for calibration. Bright, isolated stars were chosen from the SPIREX image and used to calibrate the remaining stars in the image. Their L-band magnitudes were determined from the standard star, and have an average error of ± 0.05 mags.

id	RA (J2000) (h m s)	DEC(J2000) (d m s)	m_L Mag
8	11 11 10.6	-61 17 45.2	7.4
19	11 11 19.7	-61 15 26.0	7.2
173	11 12 25.4	-61 15 11.6	7.6

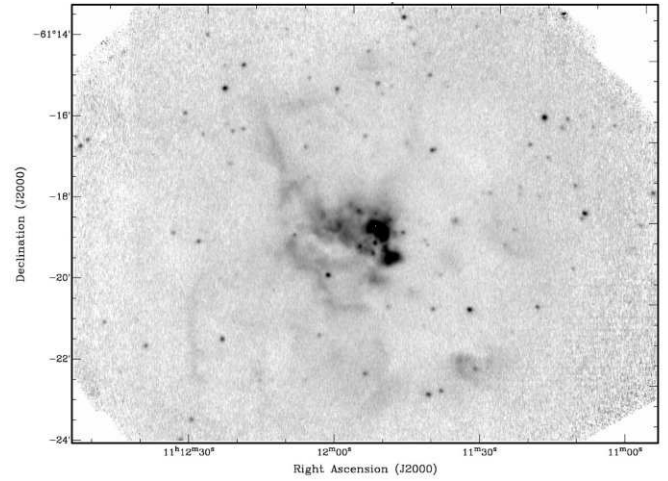
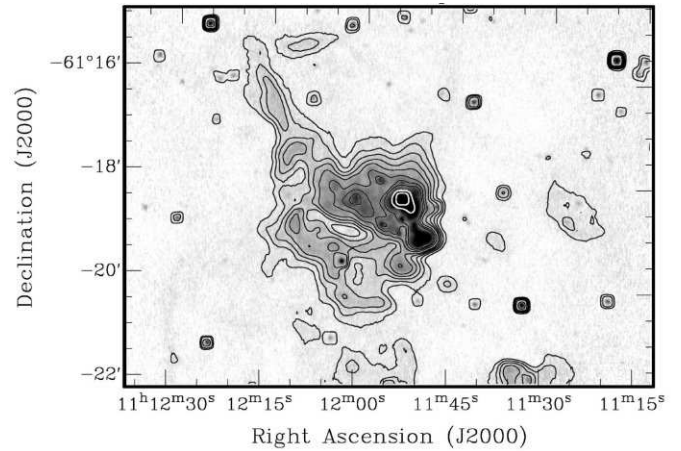
2.4. Calibration data from CASPIR

Since the SPIREX L-band image was not flux calibrated, additional observations were carried out using the Australian National University (ANU) 2.3 m telescope at Siding Spring Observatory, equipped with CASPIR (Cryogenic Array Spectrometer/Imager)(McGregor (1994)). The observations were carried out in early April 2004 together with the calibration observations for 30 Doradus (Paper I). A narrow band filter ($\lambda_{\text{central}} = 3.592 \mu\text{m}$, $\Delta\lambda = 0.078 \mu\text{m}$) was used to avoid saturation due to sky brightness, in contrast to the broader band it was possible to use with SPIREX because of the lower sky background at the South Pole. To see whether this introduced an error, the calibration stars were examined for colour variations by comparing the L-band to PAH flux ratios. These were found to be constant within the measurement uncertainties, making it possible to use the narrow band calibration data. The standard star used to calibrate the images is listed in Table 1 and the stars in the SPIREX image used to determine the zero-point correction are listed in Table 2. The individual error for the calibrated stars is ~ 0.05 mags which leads to a weighted error in the zero-point correction of ~ 0.03 mags and is included in all subsequent error calculations.

3. Results

3.1. Photometry

The L-band image of RCW 57 from SPIREX is shown in Figure 1 and an enlargement of the central region overlaid with contour lines showing the nebulosity is shown in Figure 2. The same steps to obtaining the photometry were undertaken as described for 30 Doradus in Paper I, including fitting coordinates using the *Karma* package³, running *IRAF/daophot* to get the photometry and adding 400 artificial stars using *addstar* to estimate the errors. This last step resulted in a 90% completeness limit of 11.2 mag in the L-band. The individual errors for the L-band magnitudes were given by *IRAF/daophot*. Matching

**Fig. 1.** SPIREX L-band ($3.5 \mu\text{m}$) image of RCW 57. Total on-source integration of 60 minutes; effective resolution $2.6''$; pixel scale $0.6''$; 90% completeness limit at 11.2 mag; faintest star detected 13.5 mag.**Fig. 2.** Enlargement of the central region of RCW 57 at L-band ($3.5 \mu\text{m}$) with contours showing the nebulosity. Contour levels are 0.03, 0.2, 0.4, 0.7, 1.0, 1.7, 2.3, 3.0, 8.3 and 20 mJy/arcsec^2 .

sources not in the 2MASS PSC catalogue with photometry performed on the 2MASS K_s -band atlas images resulted in an additional 17 matches.

The mosaiced SPIREX image suffered from irregular distortions (in the upper most left part of the image a recognizable pattern of 3 stars was $8''$ off). These were however small over the largest part of the image, and the L-band data could carefully be matched with the PSC and K_s -band images by marking the sources in the images and then selecting matches ‘by hand’, taking local distortions into account. Table 3 lists the statistics for detections in the various bands including the statistics when applying the 90% completeness limit.

3.2. Sensitivity

The detection threshold was taken to be three times the standard deviation σ_{sky} of a typical region of sky near each source. This resulted in a limit of ~ 12 mag at L-band, corresponding to

³ <http://www.atnf.csiro.au/karma/>

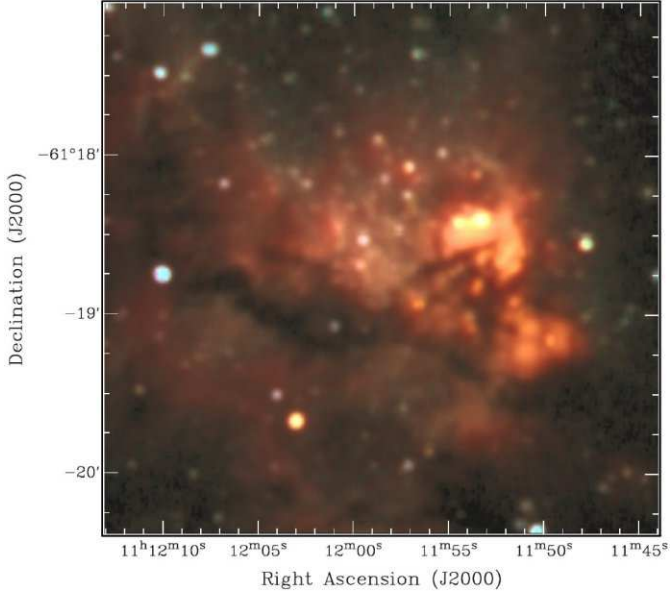


Fig. 3. HK_sL (Blue=H, Green= K_s , Red=L) composite colour image of RCW 57 created using 2MASS and SPIREX images. Regions bright in the L-band ($3.5\mu\text{m}$) can be seen in red or orange, indicating the presence of young stellar objects. Prominent dust lanes are also apparent.

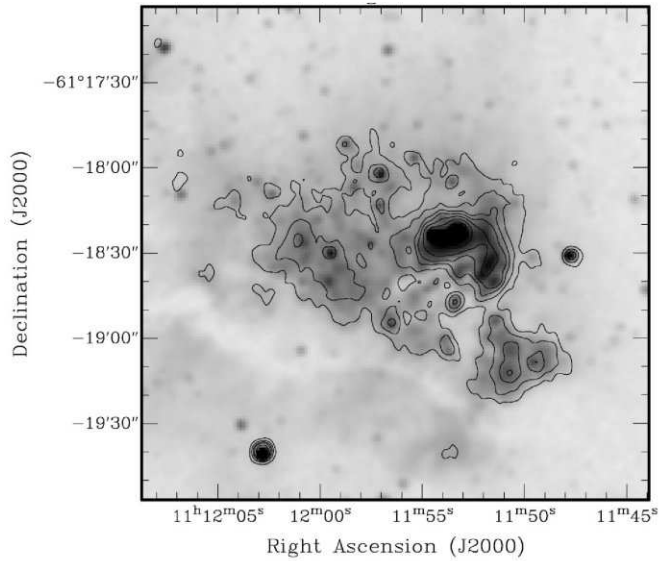


Fig. 4. Contour map of the emission measured through the H_2 Q-branch $2.42\mu\text{m}$ narrow band filter, overlaid on the 2MASS image of the K_s band emission from the central of RCW 57. Contours levels are at $0.8, 1.5, 2.2, 2.9, 4.3, 7.2$ and $13 \times 10^{-4} \text{ Jy arcsec}^{-2}$.

the 84% completeness limit. The faintest source detected has a magnitude of $m_L=13.5$ (69% completeness limit). However, only sources above the 90% completeness limit at $m_L=11.2$ mag are included in the determination of the IR-excess fraction (§ 4.2).

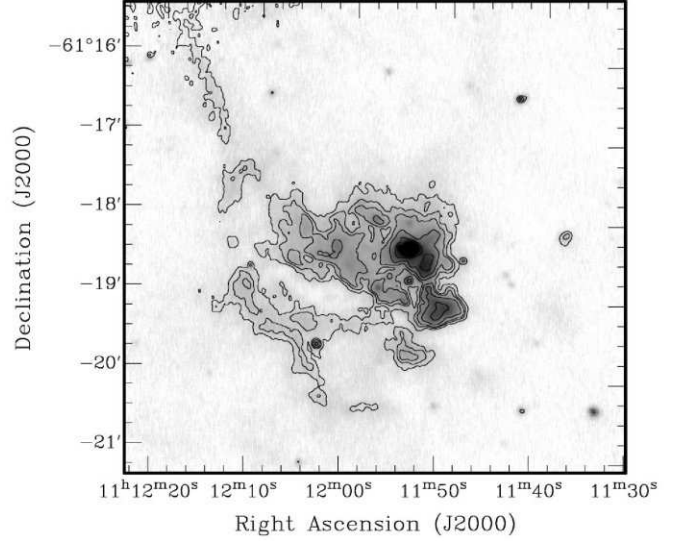


Fig. 5. Contour map of the emission measured through the PAHs $3.3\mu\text{m}$ narrow band filter, overlaid on the L-band image of RCW 57. Contours levels are at $2.2, 3.9, 5.7, 10$ and $19 \times 10^{-3} \text{ Jy arcsec}^{-2}$ for continuum, or equivalently $4.4, 8.0, 12, 20$ and $38 \times 10^{-17} \text{ W m}^{-2} \text{ arcsec}^{-2}$ if it is line emission.

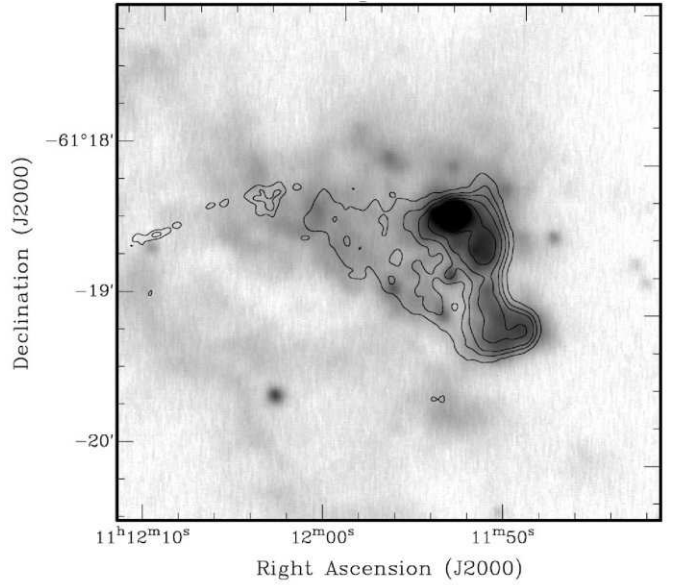


Fig. 6. Contour maps of the emission measured through the $\text{Br } \alpha$ $4.05\mu\text{m}$ narrow band filter, overlaid on the L band image of the central region of RCW 57. Contour levels are at $3.2, 4.9, 6.5, 9.8, 16, 23$ and $61 \times 10^{-2} \text{ Jy arcsec}^{-2}$.

3.3. Foreground contamination

Unfortunately off-source comparison images were not available for the SPIREX data. We therefore estimated the contamination by foreground stars using the $(J-K_s)$ colours of the stars, to determine a limiting $(J-K_s)$ colour due to interstellar reddening. Assuming that sources that are part of RCW 57 are additionally reddened, excluding all sources bluer than the $(J-K_s)$ limit gives a first order estimation of the number of foreground stars. Figuerêdo et al. ((2002)) use the star HD 97499 to de-

termine the interstellar component of the reddening to RCW 57. This results in an extinction parameter of $A_K=0.43$ which in turn gives a limiting $(J-K_s)$ colour of 0.7. This limit corresponds also to a gap in the J vs $(J-K_s)$ diagram for RCW 57, indicating main sequence stars between the source and Earth on the blue side of the gap and the stars belonging to RCW 57 or further away on the right side of the 0.7 $(J-K_s)$ colour limit. Applying this limit to the sources detected in RCW57 results in 17 potential foreground stars. Of these, 3 have moderate IR-excess ($(K_s-L)<2$) and 7 have larger excess ($(K_s-L)\sim 3-5$). The extreme red colours in potential foreground stars is surprising. However, a closer inspection of the K_s - and L-band images shows that the 2MASS sources possibly are foreground objects close to the position of embedded stars (on the sky), and therefore result in large (K_s-L) colours. In two cases (# 33 and #43), the J-band magnitude is only the 95% upper confidence limit (the uncertainty in the magnitude is given as ‘null’ in the PSC, indicating that the source either was not detected in J-band or is inconsistently deblended), resulting in an uncertain $(J-K_s)$ colour. Excluding these potential foreground stars decreases the disk fraction from 55% to 54% (see § 5.3). Likely foreground stars are indicated in Table 7 and are marked with boxes in Figs. 7 to 9.

3.4. Narrow Band Filters

The three narrow band images are shown in Figs. 4, 5 and 6. In all three images the contours showing the emission through the line filters are similar to the nearby continuum images they are overlaid on. Indeed, there is no clear evidence for line emission in either the H_2 or Br α images, although this does not preclude their presence.

Oliva & Moorwood ((1986)) report a detection of $2.6 \times 10^{-13} \text{ erg cm}^{-2} \text{ s}^{-1}$ through a $30''$ beam centred on RCW 57 for the H_2 Q-branch emission, with the flux falling to approximately one tenth that value a beam away. Their measurements were through a CVF of similar spectral resolution to the narrow band filter we employed, with the line being approximately 10% of the continuum. This would not be apparent in our image without careful continuum subtraction from the narrow band image. While H_2 emission is indeed likely present in RCW 57, all we can conclude is that it is not distinguishable from the continuum in a narrow band filter image. There are no extended regions of bright pure H_2 line emission evident.

Similarly, we cannot distinguish any Br α emission from the continuum at $4\mu\text{m}$ in a narrow band filter, although again this line is most likely present. Moorwood & Salinari ((1983)) report a detection of Br α $10''$ S of IRS1, but at a level that is about 10% of the continuum level we measure. They also report a detection of Br α on IRS1 itself, though at a level inconsistent with an upper limit of McGregor et al. ((1984)). In either case, the level would not be distinguishable from the strong continuum from IRS1 in a narrow band filter.

We can, however, report a clear detection of PAHs emission from RCW 57. While the diffuse emission in the PAHs and L band images are similar in morphology, with extended emission around IRS1 and a filament extending from it to the

Table 3. Number of detections in the different bands. The first column gives the total number of detections in the SPIREX image. The second column gives the number of stars that could be matched with the 2MASS PSC. Column three lists the number of stars additionally matched by comparison of the K_s - and L-band images. The last column lists the number of stars only found in the SPIREX L-band image. The second row lists the respective numbers for stars brighter than the 90% completeness limit. Using the $(J-K_s)$ colour limit determined in § 3.3 suggests 17 of the stars detected at JHK_sL are likely foreground stars.

	Total	JHK _s L	K _s L	L
all stars	251	201	17	33
$m_L < 11.2$ (90% limit)	209	168	8	33

NE, the contrast of the diffuse emission to the stellar sources is clearer through the PAHs filter than through the L band filter. A quantitative comparison suggests that typically about one third of the diffuse flux measured in the L band filter must come from the PAHs feature at $3.3\mu\text{m}$. It is likely that scattered continuum dominates the remaining diffuse emission at L band, although we cannot demonstrate that from the data here. The PAHs emission is presumably fluorescently excited by the far-UV photons also generated by the ionizing source(s) which excites the HII region. As can be seen in our Figure 5, typical fluxes for the $3.3\mu\text{m}$ PAHs emission are around $10^{-16} \text{ W m}^{-2} \text{ arcsec}^{-2}$ in the nebosity.

4. Analysis

4.1. Colour-colour and colour-magnitude diagrams

Figs. 7 to 9 show the colour-colour and colour-magnitude diagrams. Fig. 7 shows the $(J-H)$ colour vs. (K_s-L) colour, Fig. 8 the $(J-H)$ vs. $(H-K_s)$ colours and Fig. 9 the L-band magnitude vs. (K_s-L) colour. The diagrams were created using the JHK_s data from 2MASS and the L-band data from the SPIREX image. Only sources above the 90% completeness limit were included. The main sequence (thick solid line) for spectral types O6-8 to M5 and the giant branch (thin solid line) for spectral types K0 to M5 are plotted in each diagram. The sequences were plotted using their intrinsic colours (Koorneef (1983)) and their absolute visual magnitudes (Allen (1973)). Reddening vectors up to an extinction of $A_V=30$ mags are plotted as dashed lines, assuming an extinction law $\propto \lambda^{-1.7}$. The distance modulus used was 12.4 magnitudes, corresponding to the distance of 3 kpc to RCW 57. The crosses in the lower right corners indicate the mean errors for the stars in each figure.

4.2. Fraction of reddened sources

The fraction of reddened sources was determined taking the individual errors for each star into account. Stars which lie at least 1σ error to the right and below the reddening band are counted as having an IR-excess and are marked with the star symbol. IR-excess stars in the JHK_sL plane are marked with the same symbol in Figs. 8 and 9 as well. In Figure 9, stars that

are additionally only detected in K_s and L (diamond shaped symbols) are included. Stars only detected in the L-band can be included by providing a lower limit for the (K_s -L) colour using the 2MASS sensitivity limit at K_s (14.3 mag). These are indicated as circles and lie to the right of their positions in the colour-magnitude diagram. By comparing the location of the stars in Fig. 9 to the location of already identified IR-excess sources (star shaped symbols), it is possible to also estimate which of the stars seen only at K_s and L also have an IR-excess. Of the 8 stars that lie above the 90% completeness limit, 6 occupy this region and so are counted as having an IR-excess. The 33 stars only detected in the L-band also lie in the region occupied by the IR-excess stars and therefore all of these are counted as having an IR-excess. The statistics are listed in Table 4. The uncertainty in the number of stars with IR-excess is determined by counting the number of IR-excess sources when assuming a 2σ distance to the reddening band. The variation in this number gives an estimate of the uncertainty in IR-excess sources. This procedure excludes four sources from the JHK_sL data set. The sources only detected at K_s and L, and only at L, are not affected by this consideration. Thus, the determined fraction of IR-excess sources is $55 \pm 2\%$. The JHK_s data alone (Fig. 8), would yield only 25 IR-excess sources, compared to 75 excess sources in the JHK_sL diagram. This would lead to a considerable underestimation of the CDF. Our JHK_s diagram looks similar to the one presented by Figuerêdo et al. ((2002)) (their Fig. 4). The majority of sources lie along the reddening vector, with several sources displaying clear IR-excess at $(H-K_s) > 1.5$. Previous determinations of the fraction of sources with IR-excess in JHK_s colour-colour diagrams (Persi et al. (1994)), show that $>70\%$ of the sources have significant IR-excess. This is much higher than the fraction of excess sources determined here. However, the region covered in Persi et al. is only 340×340 square arc seconds, compared to a radius of ~ 440 arc seconds for the region covered in this paper. If an area equal to the region in Persi et al. ($\sim 3'$ in radius) is considered, the fraction of IR-excess sources increases to $79 \pm 2\%$ (Table 5 and § 5.3). The determination of sources not part of RCW 57 is only a first order estimate (§ 3.3). In particular, the estimate is a lower limit on the CDF since it may not exclude all potential background stars. Contamination from background stars is likely to be more significant in the outer regions of the image where these are not hidden behind the molecular cloud, so resulting in a lower CDF.

4.3. Luminosity Function

Figs. 10 and 11 show the luminosity function for all sources in RCW 57, and IR-excess sources, respectively. Vertical lines indicate the 90% completeness limit. Both diagrams cover the range from $m_L = 7.5$ -13.5 and peak at $m_L \sim 10$. The distribution is somewhat higher and narrower when only taking IR-excess sources into account (Fig. 11). Comparing the L-band luminosity function with the L-band magnitudes of main sequence stars, the diagrams cover the range from spectral types A3 to O5 and peak at early type B stars. Using the spectral types, it is possible to make crude estimates of the stellar masses. For

Table 4. Number of stars found with IR-excess and the reddening fraction. Numbers in the JHK_sL, K_s L and L columns are the number of stars with IR-excess found in the respective bands. These are listed assuming 1σ and 2σ distances from the reddening band. Column 5 gives the total number of sources with IR-excess at 1σ and 2σ . Column 6 gives the cluster disk fraction. Excluding possible foreground stars decreases the CDF to $\sim 54\%$. Only sources that are brighter than the 90% completeness limit (11.2 mag in L-band) are including in calculating the fraction of IR-excess sources.

distance	JHK _s L	K_s L	L	total	frac
1σ	75	6	33	114	55 ± 0.5
2σ	71	6	33	110	53 ± 0.5

early type B stars the masses lie at approximately 7-17 M_\odot (Allen (1973)). Both diagrams span a mass range of ~ 2 -60 M_\odot , confirming that RCW 57 is a high mass star forming region. However, the IR-excess might severely bias the determination of spectral types towards earlier type stars and higher masses, and so the results here can only be taken as indicative. There is a possible turnover at the 90% confidence limit in the L-band luminosity function (Fig. 10). A turnover is however not seen in the K_s -band luminosity function (KLF) (Figuerêdo et al. (2002)) and an IMF derived from the KLF gives a slope of $\Gamma = -1.62$, which is consistent with the Salpeter value (Salpeter (1955)). The KLF derived in Figuerêdo et al. included correction for non-cluster members, interstellar reddening, excess emission and photometric completeness. The resulting cluster mass integrated from their derived IMF, is $M_{cluster} = 5.4 \times 10^3 M_\odot$ (Figuerêdo et al. (2002)). This is an upper limit, as their IMF is likely to be overestimated due to excess emission. The IMF derived from the L-band luminosity function in Fig. 10 has a slope of $\Gamma = -1.42$. The integrated cluster mass for stars above the 90% completeness limit is $\sim 10^4 M_\odot$ (using $M_{lower} = 5.8 M_\odot$ and $M_{upper} = 100 M_\odot$). However, the cluster mass is dominated by contribution from stars below the completeness limit, and so is highly sensitive to the derived value for the slope of the IMF.

5. Discussion

5.1. IR-excess as an indicator of circumstellar disks

The location of stars in the JHK_sL diagram (Fig. 7) shows that $55 \pm 2\%$ of the sources lie outside of the reddening vector defined by interstellar extinction. These sources have an IR-excess, displaying more emission than simply a reddened stellar photosphere. As discussed in §1, the position of these stars in the colour-colour diagram can be explained by models of circumstellar disks around classical T Tauri stars and AeBe stars, depending on the characteristics of the disk (e.g. whether these have central holes, varying inclination angles etc) (Lada & Adams (1992)). The IR-excess stars here are therefore interpreted as stars with circumstellar disks, with the fraction of IR-excess stars taken to be equal to the cluster disk fraction (CDF). The presence of disks is also supported by the presence of the CO 2.3 μm bandhead emission or absorption, found in four ob-

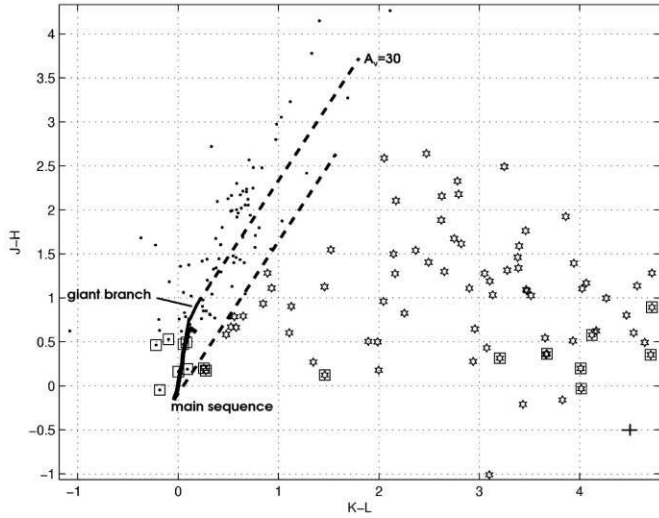


Fig. 7. JHK_sL colour-colour diagram for RCW 57. The thick solid line shows the position of the unreddened main sequence for spectral types O6-8 to M5. The thin solid line above shows the giant branch for spectral types K0 to M5 and extends from $(\text{J}-\text{H})=0.5$, $(\text{K}_s-\text{L})=0.07$ to $(\text{J}-\text{H})=0.9$ to $(\text{K}_s-\text{L})=0.19$. The dashed lines show the reddening vector up to $A_V = 30$ assuming an extinction law $\propto \lambda^{-1.7}$. Star shaped symbols are stars identified as having an IR-excess (§ 4.2). Sources in squares are have $(\text{J}-\text{K}_s) < 0.7$ (see § 3.3). The cross in the lower right of the diagram indicates the mean errors for all stars. 209 stars lie above the 90% completeness limit and 75 of these lie outside the reddening band and are therefore considered to have IR-excess (Table 3 and 4).

jects in RCW 57 (Figueroa et al. (2002)). The preferred model for such molecular emission is that it arises from the inner portions of disks (Barbosa et al. (2003)). Such an identification has been made, for example, for CO bandhead emission seen in the massive star formation region of M17, where optical spectra of some of the stars also indicate the presence of circumstellar disks (Hanson et al. (1997); Barbosa et al. (2003)).

5.2. Spatial Distribution of IR-excess sources

The spatial distribution of IR-excess stars can be seen in Figure 12. Squares represent sources detected in all four bands, plus signs sources only found in K_s - and L-band and crosses indicate the positions of sources only found in L-band. The underlying image is the SPIREX L-band image. Sources with IR-excess are mainly located in the central cluster and follow the nebulous arcs outside the cluster. Stars found in all four bands dominate the cluster, while stars only found in L-band predominantly lie in the nebulous arcs away from the centre. However, four of the six reddest stars lie in the central cluster (labelled #220, #227, #229 and #230 in Fig. 12) (§ 5.4). Table 5 shows how the CDF varies at increasing radii from the centre, and Table 6 shows how the CDF and surface density of all detected stars and IR-excess stars varies in regions at increasing distances from the centre. There is a slight increase in disk fraction and density at a distance of 3'-4' which coincides with the

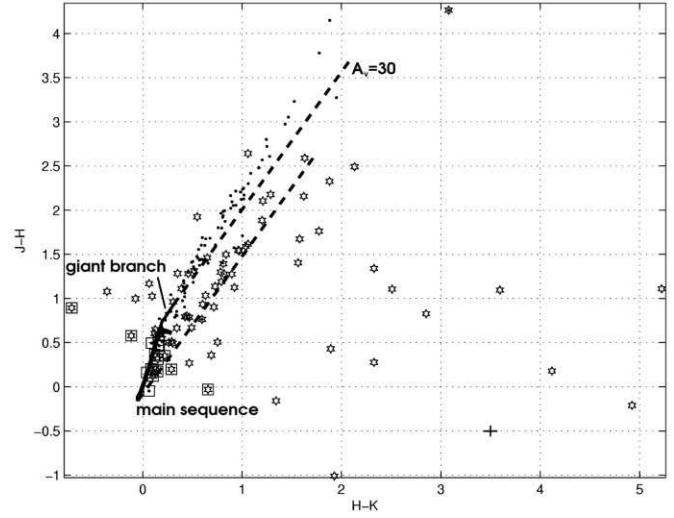


Fig. 8. JHK_s colour-colour diagram for RCW 57. The same symbols as in Figure 7 are used. The giant branch extends from $(\text{H}-\text{K}_s)=0.13$ to 0.31 with the same values for $(\text{J}-\text{H})$ as in the previous figure. The cross in the lower right corner indicates the mean error for all stars. The diagram shows the same sources as in the JHK_sL diagram using only the JHK_s -band data. Here the stars are clearly less separated than sources with IR-excess compared to using the L-band data. In this diagram only 25 sources would be classified as having IR-excess, compared to 75 in Figure 7, leading to an underestimate of the cluster disk fraction.

Table 5. Cluster Disk Fraction as a function of angular distance from the centre of RCW 57 (central coordinates are RA 11h11m53.41s, Dec -61°18'22.5'') based on the fraction of stars with an IR excess within each radius.

radius (arcmin)	CDF %
<1	95±1
<2	90±1
<3	79±2
<4	73±2
<5	66±1
<6	62±2
<7	58±2
>7	55±2

nebulous arcs to the northeast and east of the central cluster. Figueroa et al. ((2002)) find a gradient in the spatial distribution of near IR $(\text{H}-\text{K})$ colour indices towards the southwest. They suggest that this indicates a progression of star formation from the northeast to the southwest. Fig. 12 however shows IR-excess sources throughout the source, favoring star formation without any particular preferred gradient.

5.3. The Cluster Disk Fraction

The cluster disk fraction determined here, based on the colour-colour and colour-magnitude diagrams (Figs. 7 to 9) for the entire region of the image, is $\sim 54\%$ when excluding potential

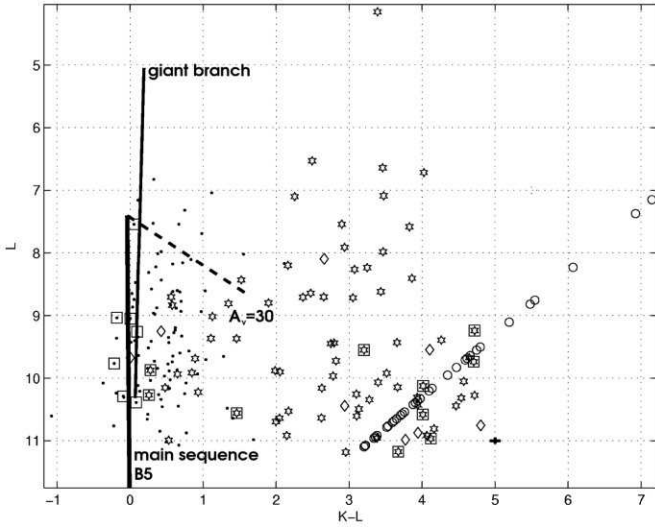


Fig. 9. Infrared L vs (K_s-L) colour-magnitude diagram for RCW 57. The thick solid line shows the main sequence for spectral types B5 and earlier, the thin solid line the giant branch for the same spectral types as in the other diagrams. The dashed line shows the reddening vector up to $A_V=30$. Star shaped symbols are the same IR-excess sources as in Figure 7. Diamond shaped symbols are stars only detected in K_s - and L-band and circles show the lower (K_s-L) limit for stars only detected in L-band (§ 4.2). Squares indicate possible foreground stars with $(J-K_s)<0.7$; § 3.3. The cross in the lower right corner indicates the mean error for all stars. 6 of the 8 stars detected in K_s and L occupy the same region as the stars with IR-excess from Figure 7. All 33 stars detected only in L-band are also in the region. These stars are also classified as IR-excess sources and are counted towards the total disk fraction (Table 4).

foreground stars (Table 4). However, as discussed earlier this is probably a lower limit due to the contamination of background sources in the outer regions of the image. The CDF together with the ages of the cluster, the CDF can give information about the evolution and lifetime of circumstellar disks. In particular, since RCW 57 is a region of massive star formation (see § 1.2 and § 4.3), it is possible to gain valuable information about the formation of massive stars and their circumstellar disks. Unfortunately, the age of RCW 57 is not well known. However, there are several indicators for recent and ongoing star formation, such as CO $2.3 \mu\text{m}$ bandhead emission and absorption, the detection of CH_3OH and H_2O maser sources and the clustering of IR-excess sources in the central region (§ 1.2 and § 5.2). Within a radius of $\sim 4'$ of the centre of the cluster, the fraction of sources with an IR-excess is $\sim 73\%$ (Table 5). This high IR-excess fraction, interpreted as the cluster disk fraction (CDF) (§ 5.1), suggests that the region is young. These signs of early stages of star formation, combined with the fast evolution timescales for massive pre-main sequence stars (on the order of 10^5 to 10^6 years), indicates an upper limit for the age of RCW 57 of ~ 1 -2 Myr, and an age spread within this limit.

In Fig. 13, the resulting CDF and age of RCW 57 are compared to earlier JHKL surveys of clusters in the Galaxy (Haisch et al. (2001)) and the results for 30 Doradus from

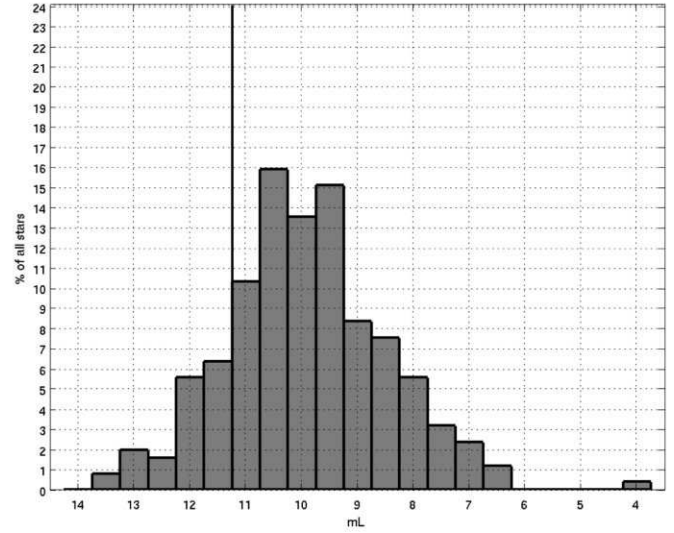


Fig. 10. L band luminosity function of all stars detected at L-band in the SPIREX image of RCW 57. Stars are detected down to $m_L \sim 13.5$, corresponding to unreddened A5 stars at the distance of RCW 57. The upper limit is $m_L \sim 4$. O5 type and earlier stars correspond to an L-band magnitude $m_L \sim 7.5$. The distribution peaks at $m_L \sim 10$ indicating early type B stars. Based on the spectral types the mass range is from 2-60 M_\odot and peaks at 7-17 M_\odot . The vertical line shows the 90% completeness limit.

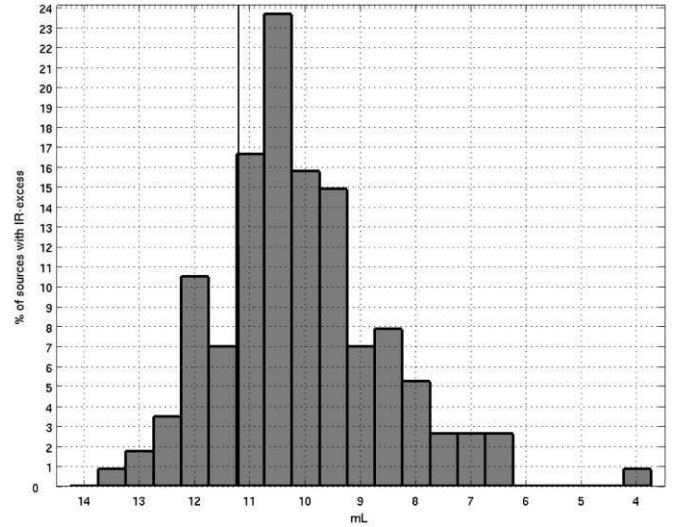


Fig. 11. The percentage of all sources with an IR-excess within each magnitude interval. The width of the distribution is narrower than in Figure 10, but covers the same range of spectral types and masses. The vertical line shows the 90% completeness limit.

Paper I. For the purpose of comparison we have assumed an age for RCW 57 of 1.5 ± 1 Myrs. The data from Haisch et al. was determined in a similar way to this paper using JHKL colour-colour diagrams. The ages for the Trapezium, IC 348, NGC 2264 and NGC 2024 were determined using pre-main-sequence (PMS) tracks, the ages for NGC 2362 and NGC 1960

Table 6. Variation of the cluster disk fraction and the surface density of sources in annuli at increasing angular distance from the centre (same central coordinates as in Table 5). The disk fraction decreases with increasing angular distance, though rises slightly however at a distance of 3-4 arcmin. The surface density of all stars and IR-excess stars behaves similarly. The slight increase coincides with the nebulous arcs to the north-east and east of the cluster seen in Figure 12, where many of the sources only detected in L-band lie. Errors in the values for the surface density are ± 0.1 sources per arcmin².

distance (arcmin)	fraction %	no. stars (per arcmin ²)	no. IR-excess sources (per arcmin ²)
0-1	95 ± 1	7	6.7
1-2	82 ± 1	1.8	1.5
2-3	59 ± 5	1.4	0.8
3-4	64 ± 3	1.6	1.0
4-5	50 ± 2	1.6	0.8
5-6	45 ± 7	0.8	0.4
6-7	27 ± 5	0.5	0.1

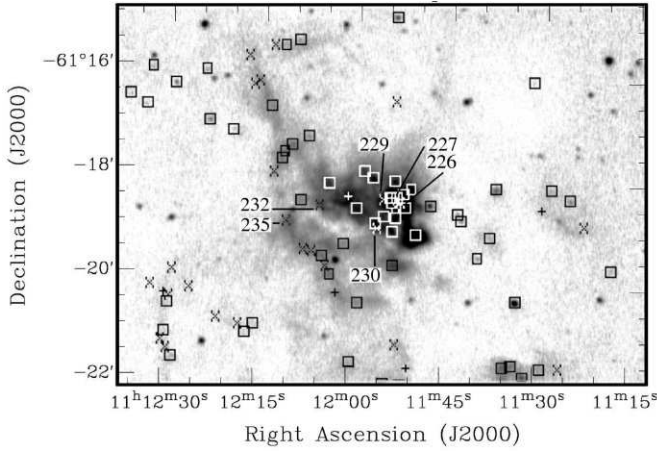


Fig. 12. Spatial distribution of IR-excess sources in RCW 57. The underlying image is the SPIREX L-band image. Squares mark stars with an IR-excess found in the JHK_sL-bands, plus signs mark stars with an IR-excess found only in the K_sL-bands and crosses mark stars with an IR-excess only found in L-band (there is no difference between white/black symbols, with the colour chosen in the nebulous regions for clarity). The stars with labels are the six reddest sources with $(K_s-L) > 5$ and are only seen in L-band.

were determined using post-main-sequence isochrone fitting in HR-diagrams (Haisch et al. (2001)). The systematic error in the upper right corner of Fig. 13 gives their estimate of the overall systematic error introduced in using different PMS tracks. The clusters included cover a range of masses and ages (0.3 Myr to 30 Myr). The error in the CDF for RCW 57 is $\pm 12\%$ and includes the error due to the uncertainty in the number of IR-excess sources ($\pm 2\%$). It also allows for the uncertainty in determining the number of foreground stars. The position of RCW 57 in Fig. 13 lies below the least-squares straight line fit to the data of Haisch et al.. However, this position on the diagram is clearly uncertain. The CDF determined includes data

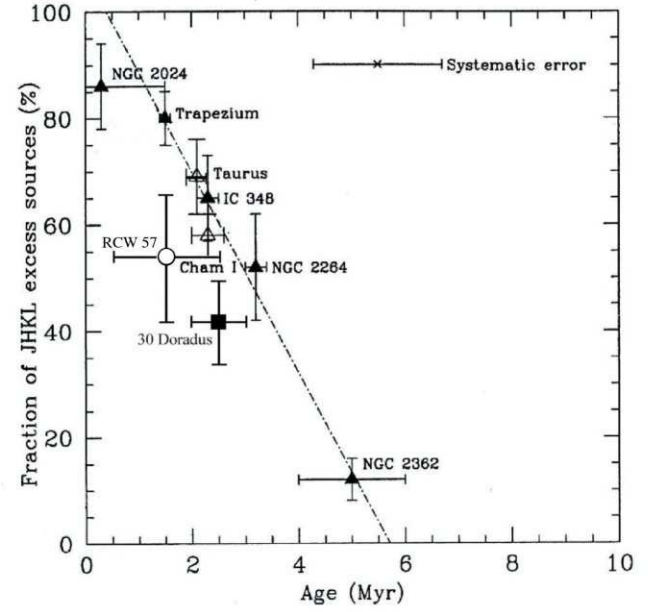


Fig. 13. Cluster disk fraction (CDF) for 7 clusters by Haisch et al. ((2001)) and 30 Doradus (Paper I) vs their mean ages. The CDFs were determined using JHK_sL data as described in the text (§ 5.3) and Paper I. The location of RCW 57 is indicated by a circle with error bars indicating the uncertainty in age and disk fraction. The dot-dashed line is the best fit determined by Haisch et al. ((2001)).

covering the entire SPIREX image, although the outer regions might be biased towards stars not belonging to RCW 57. If we only take the inner 5'-6' into account (cf. the region considered by Persi et al. (1994)), this increases the CDF to 60-65%. In the central arcmin the disk fraction is even higher, $\sim 95\%$. Considering the additional uncertainty in the age, our data is consistent with the predictions of Haisch et al. for the relation between disk fraction and age. Certainly, the disk fraction is much higher than that determined for the oldest cluster NGC 2362. However, as with 30 Doradus (Paper I), our best estimates of the disk fraction as a function of age lie below the relation determined by Haisch et al. Both 30 Doradus and RCW 57 are high mass star formation regions, where the evolution timescales for the most massive members is expected to be less than 10^6 yrs. Nevertheless, if the CDF had been determined from the JHK_s data alone, the result would have appeared to fall significantly below that of the Haisch et al. data. In RCW 57, it is possible that the external photoevaporation of circumstellar disks decreases the CDF. Lifetimes for photoevaporated disks may then be of order of 0.1 Myr (cf. Hollenbach et al. (1994)). If this is true for RCW 57, the initial disk fraction would be higher than determined here from the JHK_sL data. Extrapolating the best fit suggests that the age for circumstellar disks is no more than ~ 6 Myr.

5.4. The Cluster Core

Several very red sources ($(K_s-L) > 4.5$) lie in the central region ($r < 1'$) and in the bright arc to the southeast of the central cluster (Fig. 12). The six reddest sources ($(K_s-L) > 5$) in our data were only detected in the L-band, with their colours therefore only being lower limits. These are labelled in Fig. 12. Four of these lie in the central cluster close to the position of IRS 1 (#226, #227, #229 and #230). The remaining two lie in the bright arc to the southeast (#232 and #235). While we cannot classify these sources based on a single measurement, Barbosa et al. ((2003)) examined the cluster core in the mid-IR, determining spectral indices for 3 sources. Comparing these to indices for low mass protostars, they find two (Nos. 48, 50) that would be classified as Class I objects (two of the four sources in IRS 1 that were resolved by Barbosa et al., see § 1.2). Silicate absorption features in the spectra of the five objects seen at $10\mu\text{m}$ by Frogel & Persson ((1974)) in the inner 1.4 square arc minutes, also indicates Class I protostellar objects. Barbosa et al. ((2003)) overlay a K-band image of the cluster core with the radio continuum map by DePree et al. ((1999)). None of their sources can be associated with the radio peak emission and they suggest that the ionizing source lies hidden behind dark clouds in the line of sight. The position of the radio peak emission is confirmed by Walsh et al. ((2001)). As with the results from Barbosa et al., none of our L-band sources can be connected with the radio continuum peak, which coincides with the dark lane just south of the bright cluster core (RA 11h11m51s, Dec $-61^\circ 18' 45''$ (J2000)). The sources we see only at L-band are likely to be massive Class I protostars with circumstellar disks, still heavily embedded in their dust shells (Lada et al. (2000)). The fact that they are not detected at shorter wavelengths, and occupy the same region in the colour-magnitude diagram as the IR-excess stars, gives further support to this suggestion. In addition, 22 sources only seen in the L-band are found in the nebulous arcs further away from the cluster core (see Fig. 12). This indicates the possible presence of massive protostars in these regions as well, suggesting that massive star formation is not just confined to the central cluster.

6. Conclusions

As the second of two papers on IR-excess in massive star forming regions measured by the SPIREX telescope at the South Pole, L-band photometry for the giant HII region RCW 57 has been presented. The L-band photometry from SPIREX was combined with JHK_s data from 2MASS to determine the fraction of sources with IR-excess in JHK_sL colour-colour and colour magnitude diagrams. As for 30 Doradus, it is apparent that the JHK_s data alone would considerably underestimate the fraction of IR-excess sources, with only 25 sources classified as having an IR-excess. Using the JHK_sL data, 75 are counted towards the total fraction of stars with an IR-excess in the JHK_sL diagram. More than 50% of detected L-band sources have an IR-excess. This is, however, likely to still be a lower estimate, since foreground contamination has not fully been taken into account. Limiting the analysis to the inner $\sim 6'$ of the source, the disk fraction increases to $\sim 65\%$. The results were compared to

earlier surveys (Haisch et al. (2001)) of clusters of varying ages and masses in the Galaxy (ages between 0.3 Myr for NGC 2024 to 4.5 Myr for NGC 2362; masses down to $0.13 M_\odot$ for NGC 2024). Although the CDF for RCW 57 lies at the lower end of what is predicted by Haisch et al., it is still consistent with their data, confirming a very high initial disk fraction ($> 80\%$) and a lifetime of $\lesssim 6$ Myr. However, our results for both RCW 57 and 30 Doradus (Paper I) suggest a faster evolution of circumstellar disks around high mass stars, since the disk fractions appear to be slightly lower. This could be caused by photoevaporation of the disks due to the intense radiation environment generated by high mass stars.

Acknowledgements. This work could not have been conducted without the great help received from many colleagues within the US CARA and the Australian JACARA organisations whose efforts made the SPIREX/Abu project at the South Pole such a success, to whom we are extremely grateful. We also acknowledge the funding support from the Australian Research Council and the Australian Major National Research Facilities program that made this work possible in the first place. We thank the referee, A. P. Marston, for his perceptive comments, which have greatly improved this paper. This publication makes use of data products from the Two Micron All Sky Survey, which is a joint project of the University of Massachusetts and the Infrared Processing and Analysis Center/California Institute of Technology, funded by the National Aeronautics and Space Administration and the National Science Foundation. This research has made use of the NASA/ IPAC Infrared Science Archive, which is operated by the Jet Propulsion Laboratory, California Institute of Technology, under contract with the National Aeronautics and Space Administration.

References

- Allen, C.W. 1973, *Astrophysical Quantities*, 3rd ed., (The Athlone Press, London)
- Barbosa, C.L., Daminelli, A., Blum, R.D., Conti, P.S. 2003, *AJ*, 126, 2411
- Behrend, R., & Maeder, A. 2001, *A&A*, 373, 190
- Burton, M.G., Ashley, M.C.B., Marks, R.D., et al. 2000, *ApJ*, 542, 359
- Caswell, J.L., Batchelor, R.A., Foster, J.R., Wellington, K.S. 1989, *Austral. J. Phys.*, 42, 331
- Caswell, J.L., Vaile, R.A., Ellingsen, S.P., Whiteoak, J.B., Norris, R.P. 1995, *MNRAS*, 272, 96
- Cutri, R.M., Skrutskie, M.F., van Dyk, S., et al. 2003, *VizieR On-line Data Catalogue:II/246*. Originally published in: University of Massachusetts and Infrared Processing and Analysis Center, (IPAC/California Institute of Technology)
- DePree, C.G., Nysewander, M.C., Goss, W.M. 1999, *AJ*, 117, 2902
- Figuerêdo, E., Blum, R.D., Daminelli, A., Conti, P.S. 2002, *AJ*, 124, 2739
- Fowler, A.M., Sharp, N., Ball, W., et al. 1998, *Proc. SPIE Vol. 3354*, 1170, *Infrared Astronomical Instrumentation*, ed. Fowler, A.M.
- Frogel, J.A., & Persson, S.E. 1974, *ApJ*, 192, 351
- Goss, W.M., & Shaver, P.A. 1970, *Austral. J. Phys. Astrophys. Suppl.*, 14, 1
- Haisch, K.E., Jr., Lada, E.A., Lada, C.J. 2001, *ApJ*, 553, L153

- Hanson, M.M., Howarth, I.D., Conti, P.S. 1997, *ApJ*, 489, 698
- Hereld, M. 1994, *ExA*, 3, 87
- Hollenbach, D., Johnstone, D., Lizano, S., Shu, F. 1994, *ApJ*, 428, 654
- Kenyon, S.J., & Hartmann, L. 1995, *ApJS*, 101, 117
- Kleinmann, S.G., Lysaght, M.G., Pughe, W.L., et al. 1994, *Ap&SS*, 217, 11
- Koorneef, J. 1983, *A&A*, 128, 84
- Lada, C.J., & Adams, F.C. 1992, *ApJ*, 393, 278
- Lada, C.J., Muench, A.A., Haisch, K.E., Jr., et al. 2000, *AJ*, 120, 3162
- Maercker, M., & Burton, M.G. 2005, *A&A*, 438, 663
- McGee, R.X., & Gardner, F.F. 1986, *Austral. J. Phys. Suppl.*, 21, 149
- McGregor, P.J., Persson, S.E., & Geballe, T.R. 1984, *PASP*, 96, 315
- McGregor, P.J., Hart, J., Downing, M., Hoadley, D., Bloxham, G. 1994, *ExA*, 3, 139
- Moneti, A. 1992, *A&A*, 259, 627
- Moorwood, A.F.M., & Salinari, P. 1983, *A&A*, 125, 354
- Oliva, E., & Moorwood, A.F.M. 1986, *A&A*, 164, 104
- Persi, P., Roth, M., Tapia, M., Ferrari-Toniolo, M., Marenzi, A.R. 1994, *A&A*, 282, 474
- Rathborne, J. 2003, *Young Massive Stars: Traffic Lights for Nearby Star Formation*, PhD thesis, University of New South Wales, Sydney
- Retallack, D.S., & Goss, W.M. 1980, *MNRAS*, 193, 261
- Salpeter, E.E. 1955, *ApJ*, 121, 161
- Walsh, A.J., Bertoldi, F., Burton, M.G., Nikola, T. 2001, *MNRAS*, 326, 36
- White, G.J., & Phillips, J.P. 1983, *MNRAS*, 202, 255
- Wilson, T.L., Mezger, P.G., Gradner, F.F., Milne, D.K. 1970, *A&A*, 6, 364

Table 7. (The complete table (251 rows) is only available in electronic form at the CDS). Magnitudes for all sources (including foreground sources and sources below the 90% completeness limit) in RCW 57. Stars with measurements in all four bands are listed first. Then stars with measurements in K_s and L only, and finally stars just detected in L-band. Column 1 gives the source id. Columns 2 and 3 the RA and Dec respectively in J2000. The coordinates for sources found in all four bands are from the 2MASS point source catalogue (PSC), positions for the remaining stars are determined by reference to 2MASS images. Columns 4, 6, 8 and 10 give the JHK_s- and L-band magnitudes respectively. Columns 5, 7, 9 and 11 give the photometric errors. For sources detected in all bands, the JHK_s magnitudes and errors are taken from the 2MASS PSC. A ‘null’ as error indicates a 95% confidence upper limit for the 2MASS magnitude in the PSC. The L-band errors are combined from the errors in daophot and the errors due to the zero point correction. Sources only detected in the K_s - and L-bands have magnitudes determined from this work. For sources not detected at J, H or K_s the upper limits on these magnitudes are 15.8, 15.1 and 14.3 respectively. Stars with an IR-excess are marked with an ‘e’ in Col. 12 (comments). Likely foreground stars are marked with ‘fg’. Stars that match sources in Persi et al. ((1994)) are marked with ‘Persi’ together with the id assigned in their paper. Stars that match the MIR sources in Barbosa et al. ((2003)) are marked with ‘No’ and the id used in their paper.

id	RA (J2000) (h m s)	Dec (J2000) (d m s)	m_J	σ_J	m_H	σ_H	m_K	σ_K	m_L	σ_L	comments
1	11 10 50.0	-61 18 20.2	09.8	0.02	08.9	0.03	08.6	0.02	08.3	0.06	
2	11 10 56.8	-61 17 08.6	09.7	0.02	08.9	0.05	08.5	0.02	08.5	0.04	
3	11 10 59.1	-61 17 58.3	12.6	0.02	10.7	0.02	09.9	0.02	09.3	0.07	
4	11 10 59.9	-61 18 39.8	15.1	0.06	14.6	0.12	14.3	0.08	09.7	0.04	e
5	11 11 05.2	-61 15 32.8	10.4	0.02	09.7	0.02	09.4	0.02	09.4	0.06	
6	11 11 06.0	-61 15 05.3	11.5	0.02	10.6	0.02	10.3	0.02	10.0	0.12	
7	11 11 09.6	-61 15 36.1	11.0	0.02	10.3	0.02	10.0	0.02	10.2	0.05	
8	11 11 10.6	-61 17 45.2	08.2	0.02	07.8	0.05	07.6	0.02	07.5	0.03	fg
9	11 11 12.4	-61 15 20.4	11.4	0.02	10.8	0.02	10.7	0.02	11.4	0.04	
10	11 11 12.4	-61 19 08.9	12.1	0.02	10.4	0.02	09.7	0.02	10.1	0.05	
11	11 11 12.7	-61 17 04.9	10.6	0.02	09.6	0.02	09.3	0.02	09.0	0.05	
12	11 11 15.0	-61 15 26.5	10.5	0.02	09.7	0.02	09.2	0.02	08.9	0.04	
13	11 11 16.7	-61 21 19.7	18.1	null	13.9	0.02	12.0	0.02	10.6	0.04	
14	11 11 16.7	-61 12 51.1	08.7	0.01	07.6	0.03	07.2	0.01	06.8	0.03	
15	11 11 17.7	-61 19 39.7	12.2	0.02	12.1	0.05	12.0	0.02	10.6	0.03	e, fg
16	11 11 17.8	-61 18 00.0	10.9	0.02	10.8	0.02	10.7	0.02	11.6	0.04	
17	11 11 18.6	-61 16 25.6	11.1	0.02	10.2	0.02	09.8	0.02	09.5	0.05	
18	11 11 19.5	-61 20 09.5	12.4	0.03	10.2	0.02	09.2	0.02	08.6	0.03	
19	11 11 19.7	-61 15 26.0	08.0	0.01	07.4	0.04	07.3	0.02	07.2	0.03	
20	11 11 20.1	-61 17 24.0	12.2	0.04	11.1	0.04	10.7	0.03	10.2	0.09	
21	11 11 21.2	-61 18 43.0	14.8	0.05	13.5	0.05	12.9	0.05	12.0	0.35	
22	11 11 22.4	-61 16 07.8	10.4	0.02	09.6	0.02	09.3	0.02	09.0	0.04	
23	11 11 24.0	-61 17 22.7	11.1	0.02	10.4	0.02	10.2	0.02	10.1	0.08	
24	11 11 24.1	-61 17 12.3	12.3	0.02	11.5	0.02	10.9	0.02	10.7	0.04	
25	11 11 24.4	-61 20 49.5	17.4	null	13.6	0.03	11.8	0.02	10.5	0.04	
26	11 11 24.9	-61 18 16.6	10.5	0.02	10.3	0.02	10.2	0.02	09.9	0.05	e, fg
27	11 11 26.5	-61 13 06.6	12.8	0.03	11.1	0.02	10.5	0.02	09.9	0.09	
28	11 11 26.6	-61 18 39.8	14.4	0.04	12.0	0.03	10.9	0.03	09.7	0.04	
29	11 11 27.1	-61 17 03.9	15.0	0.05	13.7	0.06	13.1	0.05	11.7	0.09	
30	11 11 27.7	-61 16 12.7	13.9	0.03	13.6	0.08	13.5	0.07	12.1	0.11	
31	11 11 27.9	-61 17 01.4	16.4	0.15	15.7	0.14	14.8	0.14	11.7	0.05	
32	11 11 28.4	-61 18 08.6	15.3	0.06	14.3	0.05	13.6	0.08	10.5	0.08	e
33	11 11 29.3	-61 21 36.1	14.8	null	14.8	0.15	14.1	0.17	10.1	0.07	e, fg
34	11 11 30.1	-61 17 23.6	13.0	0.03	11.0	0.02	10.2	0.02	09.6	0.06	
35	11 11 31.4	-61 16 04.6	15.1	0.06	14.9	0.09	14.6	0.10	10.6	0.04	e, fg
36	11 11 31.6	-61 17 23.7	13.2	0.03	11.8	0.02	11.1	0.02	10.4	0.04	Persi 4
37	11 11 31.6	-61 22 05.1	15.7	0.15	14.5	0.15	13.7	0.11	10.6	0.09	e
38	11 11 31.7	-61 21 46.9	10.4	0.03	09.8	0.03	09.4	0.03	08.8	0.04	e
39	11 11 31.9	-61 16 12.6	14.9	0.04	14.3	0.04	13.8	0.06	11.3	0.06	
40	11 11 32.0	-61 18 06.4	14.9	0.04	14.5	0.04	14.4	0.10	12.2	0.06	
41	11 11 33.0	-61 23 51.8	11.7	0.02	09.2	0.02	08.1	0.03	07.3	0.03	
42	11 11 33.4	-61 20 19.7	16.8	null	15.7	0.22	10.4	0.02	07.5	0.03	e

Table 7. continued.

id	RA (J2000) (h m s)	Dec (J2000) (d m s)	m_J	σ_J	m_H	σ_H	m_K	σ_K	m_L	σ_L	comments
43	11 11 33.6	-61 21 35.5	14.1	null	13.2	null	14.0	0.21	09.2	0.05	e, fg
44	11 11 33.9	-61 11 35.0	09.0	0.03	08.2	0.04	07.8	0.02	07.5	0.03	
45	11 11 34.3	-61 13 16.8	12.3	0.02	10.9	0.02	10.3	0.02	09.7	0.07	
46	11 11 34.6	-61 21 36.9	13.9	0.08	12.6	0.10	11.8	0.07	08.7	0.06	e
47	11 11 35.3	-61 18 25.3	15.8	0.09	14.3	0.07	13.4	0.04	12.0	0.08	
48	11 11 36.4	-61 16 55.0	16.3	0.13	15.2	0.09	14.6	0.09	11.9	0.08	
49	11 11 36.6	-61 12 04.6	15.8	0.08	15.2	0.09	15.0	0.14	10.8	0.05	e
50	11 11 37.1	-61 18 08.6	13.6	0.04	12.0	null	11.1	null	08.7	0.05	e
51	11 11 38.0	-61 12 05.2	12.7	0.03	11.5	0.02	11.2	0.02	10.2	0.03	e
52	11 11 38.1	-61 19 04.3	12.6	0.03	12.1	0.04	11.9	0.04	09.9	0.06	e
53	11 11 38.6	-61 22 22.4	16.8	null	17.0	null	12.1	0.02	08.6	0.04	e
54	11 11 39.5	-61 11 34.9	15.6	0.08	15.0	0.08	15.1	0.17	11.0	0.04	e, fg
55	11 11 39.6	-61 13 54.6	12.3	0.04	11.5	null	11.3	0.03	11.7	0.04	
56	11 11 39.7	-61 19 30.1	16.3	null	14.5	null	13.3	0.08	10.6	0.04	e
57	11 11 39.8	-61 14 49.2	13.7	0.02	11.6	0.02	10.7	0.02	10.3	0.05	
58	11 11 41.0	-61 20 22.1	09.7	0.02	09.1	0.02	08.9	0.02	08.9	0.03	
59	11 11 41.1	-61 22 29.1	17.6	null	13.4	0.05	10.3	0.02	08.2	0.03	
60	11 11 42.5	-61 16 25.2	11.6	0.02	09.7	0.03	08.9	0.02	08.2	0.03	
61	11 11 42.5	-61 18 15.6	17.9	null	14.6	0.06	12.7	0.03	11.0	0.04	
62	11 11 42.6	-61 18 46.5	17.0	null	16.8	null	12.7	0.02	10.7	0.04	e
63	11 11 42.9	-61 12 57.2	11.8	0.02	11.0	0.02	10.6	0.02	09.9	0.08	e
64	11 11 43.2	-61 18 39.2	16.1	null	14.5	null	13.5	0.07	10.1	0.05	e
65	11 11 43.2	-61 19 15.6	16.4	null	15.0	0.10	13.9	0.06	12.9	0.15	
66	11 11 43.5	-61 14 33.5	12.7	0.04	10.6	0.03	09.6	0.02	08.9	0.04	
67	11 11 45.1	-61 14 24.3	16.5	0.15	15.0	0.09	14.3	0.09	11.0	0.04	e
68	11 11 45.4	-61 21 18.2	14.6	0.03	14.2	0.03	14.1	0.06	12.2	0.13	
69	11 11 46.2	-61 14 30.7	15.8	0.08	14.2	0.04	13.6	0.06	11.7	0.04	
70	11 11 46.9	-61 11 31.9	09.3	0.02	09.1	0.02	09.1	0.02	09.0	0.07	fg
71	11 11 47.1	-61 13 49.0	10.3	0.02	09.7	0.02	09.5	0.02	10.6	0.05	
72	11 11 47.3	-61 15 25.0	13.5	0.02	11.7	0.02	10.9	0.02	10.5	0.04	
73	11 11 47.7	-61 20 44.5	16.1	0.10	15.8	0.14	15.1	null	11.8	0.06	
74	11 11 47.7	-61 18 30.6	12.5	0.03	10.9	0.02	10.0	0.02	08.4	0.03	e, Persi 43, No 04
75	11 11 47.8	-61 16 17.3	13.4	0.04	11.6	0.03	10.7	0.02	09.7	0.05	
76	11 11 47.9	-61 13 24.7	10.2	0.02	09.7	0.02	09.5	0.02	09.8	0.05	fg
77	11 11 49.4	-61 13 09.3	10.3	0.02	08.9	0.07	08.4	0.02	08.0	0.03	
78	11 11 49.6	-61 19 08.5	14.4	null	13.3	0.29	10.7	0.15	06.7	0.06	e, Persi 45, No 11
79	11 11 50.1	-61 16 30.0	17.4	null	14.7	0.05	12.7	0.02	13.5	0.19	
80	11 11 50.2	-61 20 22.6	10.6	0.02	09.9	0.02	09.8	0.02	09.6	0.05	
81	11 11 50.2	-61 12 58.6	12.3	0.02	10.9	0.02	10.4	0.02	10.0	0.04	
82	11 11 51.1	-61 18 14.3	12.6	null	12.8	0.34	11.4	0.27	07.6	0.06	e
83	11 11 51.2	-61 14 53.5	12.8	0.02	11.2	0.02	10.5	0.02	10.8	0.04	
84	11 11 51.7	-61 22 04.0	16.2	null	15.0	null	15.0	0.17	10.9	0.11	e
85	11 11 51.8	-61 18 20.4	13.0	0.16	12.2	0.03	09.4	null	07.1	0.06	e
86	11 11 51.8	-61 14 20.5	13.0	0.02	11.4	0.02	10.8	0.02	10.3	0.12	
87	11 11 52.0	-61 18 37.4	13.6	0.10	11.9	0.15	10.1	0.12	06.6	0.06	e
88	11 11 53.2	-61 18 22.4	11.2	null	09.9	0.11	07.5	0.02	04.1	0.03	e, Persi 60, Nos. 48, 50, 60, 60b, IRS 1
89	11 11 53.3	-61 15 05.1	13.3	0.03	11.8	null	10.8	null	10.1	0.03	
90	11 11 53.3	-61 19 40.2	14.7	null	12.8	null	12.3	0.16	08.4	0.06	e
91	11 11 53.5	-61 18 04.5	13.7	null	13.2	0.16	11.3	0.08	08.3	0.05	e, Persi 62, No 52
92	11 11 53.5	-61 18 49.5	16.1	0.13	15.0	0.15	11.4	null	08.0	0.03	e, Persi 61
93	11 11 53.7	-61 19 04.5	16.1	null	13.6	null	11.5	0.10	08.2	0.04	e
94	11 11 53.9	-61 18 28.3	11.3	null	10.2	null	10.6	0.07	07.1	0.05	e
95	11 11 54.2	-61 14 50.4	11.8	0.02	10.9	0.02	10.1	0.02	09.0	0.04	e
96	11 11 54.2	-61 23 29.6	14.9	0.04	14.3	0.04	14.1	0.07	11.2	0.05	e

Table 7. continued.

id	RA (J2000) (h m s)	Dec (J2000) (d m s)	m_J	σ_J	m_H	σ_H	m_K	σ_K	m_L	σ_L	comments
97	11 11 54.3	-61 22 11.3	14.6	null	13.9	null	14.4	0.16	12.2	0.29	
98	11 11 54.4	-61 18 24.0	12.0	0.14	10.6	0.14	09.0	0.09	06.5	0.04	e
99	11 11 54.4	-61 22 04.0	10.5	0.02	09.7	0.02	09.3	0.02	08.7	0.03	e
100	11 11 54.6	-61 13 48.4	12.7	0.02	11.3	0.02	10.8	0.02	11.4	0.07	
101	11 11 54.8	-61 18 30.6	13.5	0.02	10.9	null	09.6	null	08.0	0.05	
102	11 11 55.3	-61 18 45.2	15.5	0.08	13.8	0.10	12.2	0.10	09.4	0.05	e, Persi 69
103	11 11 55.4	-61 23 09.3	14.7	0.02	12.5	0.02	11.5	0.02	11.0	0.10	
104	11 11 55.7	-61 14 20.0	16.6	0.17	15.3	0.10	15.0	0.15	10.3	0.05	e
105	11 11 56.2	-61 21 46.5	14.4	0.03	13.9	0.04	13.8	0.06	12.3	0.32	
106	11 11 56.3	-61 16 10.2	11.7	0.02	10.3	0.02	09.7	0.02	09.4	0.05	
107	11 11 56.3	-61 14 03.3	12.7	0.02	10.7	0.02	09.9	0.02	09.4	0.05	
108	11 11 56.5	-61 18 55.0	13.5	null	13.2	null	10.9	0.10	07.9	0.04	e, Persi 77, No 160
109	11 11 56.6	-61 17 18.3	13.5	0.03	12.5	0.03	11.7	0.02	11.1	0.09	Persi 79
110	11 11 56.7	-61 17 06.4	14.4	null	13.4	null	13.6	0.08	13.2	0.20	
111	11 11 57.0	-61 18 02.0	12.5	0.09	11.3	0.08	10.4	0.06	08.2	0.04	e, No 184
112	11 11 57.8	-61 14 30.6	15.0	0.07	14.5	0.08	14.2	0.09	10.3	0.08	e
113	11 11 58.3	-61 16 34.4	15.5	0.08	14.1	0.05	13.5	0.05	11.7	0.08	
114	11 11 58.3	-61 11 54.2	14.0	0.05	13.0	0.04	12.7	0.03	10.6	0.04	e
115	11 11 58.7	-61 17 51.1	13.4	0.02	12.1	0.06	11.4	0.06	08.7	0.06	e, Persi 89
116	11 11 59.4	-61 11 55.5	11.2	0.02	10.5	0.02	10.3	0.02	09.8	0.04	
117	11 11 59.5	-61 20 26.6	14.6	null	13.5	null	13.4	0.17	09.9	0.06	e
118	11 11 59.6	-61 18 39.8	12.0	0.09	11.4	0.14	10.7	0.12	08.8	0.05	e, Persi 90
119	11 11 59.9	-61 21 38.8	16.6	0.15	15.2	0.12	14.4	0.12	10.4	0.08	e
120	11 12 00.3	-61 15 27.1	14.4	0.05	12.9	0.05	12.0	0.03	11.4	0.04	
121	11 12 00.6	-61 10 50.6	10.6	0.02	09.3	0.02	08.9	0.02	08.4	0.04	
122	11 12 01.6	-61 19 16.7	16.2	null	15.4	null	14.9	0.20	10.4	0.06	e
123	11 12 02.5	-61 15 02.1	10.5	0.03	09.3	0.03	08.9	0.02	08.6	0.04	
124	11 12 02.8	-61 19 40.7	13.1	0.03	10.1	0.02	08.7	0.02	07.7	0.03	Persi 106
125	11 12 03.9	-61 19 57.9	13.8	0.04	13.3	0.07	13.1	0.08	09.4	0.06	e, Persi 110
126	11 12 04.0	-61 18 11.2	14.8	0.15	12.2	null	11.1	null	08.6	0.05	e, Persi 111
127	11 12 04.1	-61 21 11.2	13.0	0.02	10.8	0.02	10.0	0.02	09.4	0.04	
128	11 12 04.8	-61 22 45.2	16.7	null	15.6	0.12	14.5	0.08	12.0	0.07	
129	11 12 05.2	-61 21 47.6	15.0	0.03	14.6	0.05	14.7	0.10	12.3	0.06	
130	11 12 05.7	-61 19 35.0	15.0	0.05	14.7	0.04	14.4	0.11	09.7	0.05	e, fg
131	11 12 06.1	-61 22 31.7	14.0	0.04	13.7	0.05	13.7	0.05	12.3	0.08	
132	11 12 06.7	-61 22 19.3	14.3	0.03	12.0	0.02	11.0	0.02	10.3	0.07	
133	11 12 07.2	-61 12 28.3	10.5	0.02	09.7	0.02	09.5	0.02	09.4	0.03	
134	11 12 07.6	-61 17 17.3	11.4	0.03	10.8	0.03	10.6	0.04	10.2	0.06	e, Persi 177
135	11 12 08.0	-61 15 53.8	12.1	0.02	11.2	0.02	10.8	0.02	10.6	0.07	
136	11 12 08.5	-61 16 31.9	09.6	0.02	09.5	0.02	09.4	0.02	09.3	0.04	fg
137	11 12 08.6	-61 18 27.9	15.6	null	15.0	null	14.9	0.19	10.3	0.07	e
138	11 12 08.8	-61 14 23.9	10.8	0.02	10.6	0.02	10.5	0.02	10.3	0.03	e, fg
139	11 12 09.8	-61 15 23.6	17.0	null	14.6	0.09	12.7	0.05	10.0	0.06	e
140	11 12 10.0	-61 18 44.2	08.9	0.02	08.9	0.04	08.9	0.02	09.0	0.04	fg, Persi123
141	11 12 10.0	-61 25 43.6	10.7	0.02	09.1	0.02	08.4	0.02	08.0	0.04	
142	11 12 10.2	-61 17 26.7	11.2	0.02	10.6	0.02	10.5	0.03	09.4	0.06	e, Persi 125
143	11 12 10.9	-61 17 34.9	15.7	0.17	13.5	null	12.2	null	09.4	0.06	e
144	11 12 11.2	-61 17 41.5	14.6	null	13.6	null	13.7	0.16	09.4	0.06	e
145	11 12 12.1	-61 14 15.5	12.6	0.03	11.1	0.02	10.6	0.02	10.0	0.03	
146	11 12 12.4	-61 15 28.8	16.5	0.15	15.4	null	14.6	null	10.1	0.07	e
147	11 12 12.8	-61 15 13.3	17.5	null	13.7	0.02	12.1	0.02	11.7	0.04	
148	11 12 13.0	-61 14 44.6	12.0	0.02	11.3	0.02	11.1	0.02	13.0	0.25	
149	11 12 13.3	-61 13 38.0	12.5	0.02	10.9	0.02	10.2	0.02	09.8	0.04	
150	11 12 13.7	-61 22 21.4	14.4	0.02	12.6	0.02	11.6	0.02	10.9	0.04	

Table 7. continued.

id	RA (J2000) (h m s)	Dec (J2000) (d m s)	m_J	σ_J	m_H	σ_H	m_K	σ_K	m_L	σ_L	comments
151	11 12 14.3	-61 16 43.9	13.2	0.02	12.9	0.05	12.8	0.06	09.5	0.06	e, fg
152	11 12 14.3	-61 12 55.7	13.0	0.04	11.4	0.03	10.9	0.02	09.9	0.03	
153	11 12 15.4	-61 22 50.2	16.2	null	15.5	0.14	14.8	0.14	11.8	0.09	
154	11 12 15.7	-61 21 04.0	15.5	0.08	14.1	0.04	13.6	0.06	10.3	0.03	e
155	11 12 15.9	-61 22 23.4	13.0	0.03	11.2	0.02	10.4	0.02	09.6	0.06	
156	11 12 16.0	-61 21 42.9	15.9	null	15.2	0.11	14.5	0.13	11.8	0.07	
157	11 12 16.3	-61 21 56.4	13.3	0.03	11.8	0.03	11.3	0.02	10.8	0.04	
158	11 12 17.0	-61 21 14.1	15.4	null	13.9	0.06	13.1	0.07	10.9	0.13	e
159	11 12 17.3	-61 13 36.3	12.3	0.02	11.0	0.02	10.6	0.02	09.7	0.04	e
160	11 12 19.1	-61 20 12.1	15.3	0.08	14.8	0.08	14.6	0.10	13.3	0.18	
161	11 12 20.0	-61 19 50.5	14.0	0.04	13.7	0.04	13.6	0.06	12.4	0.05	
162	11 12 20.5	-61 17 07.9	15.3	0.07	15.0	0.07	14.8	0.13	11.2	0.04	e, fg
163	11 12 21.1	-61 11 56.0	10.9	0.03	10.6	0.02	10.2	0.02	08.8	0.05	e
164	11 12 21.3	-61 16 10.5	10.0	0.02	09.3	0.02	09.2	0.02	09.4	0.05	
165	11 12 21.6	-61 19 48.0	11.1	0.03	10.6	0.02	10.5	0.02	10.4	0.08	fg
166	11 12 21.7	-61 14 35.2	10.4	0.02	09.1	0.02	08.6	0.02	08.2	0.04	
167	11 12 23.5	-61 16 15.2	13.8	0.03	11.2	0.03	10.0	0.02	09.3	0.05	
168	11 12 23.9	-61 17 03.4	12.9	0.03	11.8	0.03	10.8	0.02	09.4	0.05	e
169	11 12 24.0	-61 21 25.2	11.7	0.02	09.7	0.02	08.8	0.02	08.2	0.03	
170	11 12 24.3	-61 23 58.2	13.2	0.03	11.2	0.02	10.4	0.02	09.9	0.07	
171	11 12 24.7	-61 16 04.9	16.6	0.16	14.4	0.06	12.8	0.05	10.2	0.04	e
172	11 12 24.9	-61 19 55.7	10.6	0.02	10.6	0.02	10.5	0.02	11.2	0.04	
173	11 12 25.4	-61 15 11.6	11.2	0.02	09.1	0.02	08.2	0.03	07.5	0.03	
174	11 12 25.6	-61 14 38.0	12.0	0.04	10.6	null	10.1	null	09.8	0.03	
175	11 12 27.0	-61 19 55.0	14.2	0.04	13.0	0.04	12.2	0.04	11.6	0.05	
176	11 12 28.2	-61 21 44.9	15.2	0.25	13.6	null	12.5	null	09.7	0.03	e
177	11 12 29.4	-61 13 54.1	11.4	0.03	10.0	0.02	09.5	0.02	09.3	0.03	
178	11 12 29.6	-61 19 01.9	12.6	0.03	10.3	0.02	09.2	0.02	08.6	0.04	
179	11 12 29.6	-61 16 21.8	12.3	0.02	11.4	0.02	10.8	0.02	09.9	0.04	e
180	11 12 29.6	-61 23 27.1	12.4	0.03	10.4	0.02	09.5	0.02	08.8	0.04	
181	11 12 29.7	-61 24 22.1	13.5	0.02	11.3	0.02	10.3	0.02	09.6	0.08	
182	11 12 29.7	-61 20 42.9	14.3	null	15.3	0.19	13.4	null	10.3	0.04	e
183	11 12 30.1	-61 21 14.3	14.9	0.19	14.5	0.20	13.8	0.16	10.1	0.04	e
184	11 12 31.7	-61 23 59.1	12.5	0.02	10.3	0.02	09.3	0.02	08.6	0.04	
185	11 12 32.9	-61 14 13.8	11.9	0.02	10.7	0.02	10.2	0.02	10.3	0.04	
186	11 12 33.4	-61 15 52.1	11.6	0.02	10.2	0.02	09.4	0.02	08.8	0.04	
187	11 12 33.4	-61 16 05.3	16.2	null	13.6	0.04	12.0	0.02	09.9	0.03	e
188	11 12 34.3	-61 16 48.7	12.7	0.02	12.0	0.02	11.5	0.02	11.0	0.05	e
189	11 12 34.9	-61 18 51.5	14.0	0.02	11.2	0.02	09.9	0.02	08.9	0.06	
190	11 12 37.0	-61 16 39.1	16.0	0.10	13.9	0.05	12.7	0.04	10.5	0.04	e
191	11 12 39.6	-61 21 41.7	10.3	0.02	09.2	0.02	08.8	0.02	08.7	0.05	
192	11 12 41.6	-61 21 05.4	11.8	0.02	10.8	0.02	10.3	0.02	10.2	0.04	
193	11 12 48.4	-61 21 10.4	13.0	0.03	10.8	0.03	09.8	0.02	09.2	0.04	
194	11 12 49.1	-61 18 13.2	10.9	0.02	10.4	0.02	10.2	0.02	10.3	0.05	fg
195	11 12 53.2	-61 16 41.0	14.2	0.03	11.1	0.02	09.6	0.02	08.6	0.04	
196	11 12 54.6	-61 16 51.0	10.5	0.02	09.2	0.02	08.7	0.02	08.6	0.10	
197	11 12 55.6	-61 16 38.0	14.0	0.03	11.3	0.02	10.1	0.02	09.7	0.07	
198	11 12 58.7	-61 16 38.8	12.9	0.03	09.7	0.02	08.2	null	07.0	0.03	
199	11 12 59.0	-61 20 10.6	12.4	0.03	10.4	0.02	09.5	0.02	08.9	0.04	
200	11 13 01.4	-61 16 53.6	11.9	0.02	10.4	0.02	09.9	0.02	09.2	0.07	
201	11 13 03.3	-61 17 48.6	12.6	0.02	10.1	0.02	08.9	0.02	08.1	0.04	
202	11 11 16.0	-61 15 40.2	-	-	-	-	09.7	0.01	09.3	0.05	
203	11 11 24.1	-61 16 41.7	-	-	-	-	14.4	0.13	12.1	0.12	
204	11 11 25.9	-61 16 28.8	-	-	-	-	15.6	0.40	12.1	0.09	

Table 7. continued.

id	RA (J2000) (h m s)	Dec (J2000) (d m s)	m_J	σ_J	m_H	σ_H	m_K	σ_K	m_L	σ_L	comments
205	11 11 28.7	-61 21 54.9	-	-	-	-	14.8	0.21	11.0	0.14	e
206	11 11 29.3	-61 18 33.1	-	-	-	-	15.6	0.39	10.8	0.11	e
207	11 11 35.9	-61 23 00.6	-	-	-	-	14.5	0.16	11.4	0.09	
208	11 11 48.6	-61 14 23.7	-	-	-	-	15.9	0.54	12.8	0.14	
209	11 11 50.1	-61 21 41.9	-	-	-	-	14.8	0.23	10.9	0.12	e
210	11 11 51.9	-61 14 40.7	-	-	-	-	14.6	0.17	13.2	0.09	
211	11 12 00.8	-61 18 26.2	-	-	-	-	10.8	0.09	08.1	0.05	e
212	11 12 01.8	-61 20 19.2	-	-	-	-	13.7	0.17	09.5	0.05	e
213	11 12 08.2	-61 14 48.7	-	-	-	-	09.7	0.02	09.7	0.03	
214	11 12 20.0	-61 22 40.6	-	-	-	-	14.9	0.18	11.5	0.05	
215	11 12 20.7	-61 20 52.4	-	-	-	-	15.3	0.27	11.5	0.06	
216	11 12 27.3	-61 20 13.5	-	-	-	-	12.7	0.04	11.5	0.04	
217	11 12 29.7	-61 20 32.1	-	-	-	-	13.4	0.08	10.4	0.04	e
218	11 12 31.3	-61 20 42.3	-	-	-	-	11.7	0.02	12.0	0.08	
219	11 11 22.3	-61 18 49.1	-	-	-	-	-	-	11.1	0.14	e
220	11 11 25.6	-61 21 36.9	-	-	-	-	-	-	10.7	0.12	e
221	11 11 30.1	-61 13 42.7	-	-	-	-	-	-	10.8	0.04	e
222	11 11 50.1	-61 22 38.5	-	-	-	-	-	-	10.4	0.09	e
223	11 11 52.2	-61 22 45.4	-	-	-	-	-	-	10.4	0.10	e
224	11 11 52.3	-61 22 57.0	-	-	-	-	-	-	10.9	0.15	e
225	11 11 52.4	-61 21 14.7	-	-	-	-	-	-	10.2	0.08	e
226	11 11 52.4	-61 18 28.2	-	-	-	-	-	-	07.2	0.06	e
227	11 11 53.2	-61 18 33.6	-	-	-	-	-	-	07.4	0.05	e
228	11 11 53.7	-61 16 30.6	-	-	-	-	-	-	10.6	0.04	e
229	11 11 55.3	-61 18 26.2	-	-	-	-	-	-	08.2	0.05	e, Persi 68
230	11 11 56.1	-61 19 00.5	-	-	-	-	-	-	08.8	0.05	e, Persi 71
231	11 12 04.4	-61 19 46.5	-	-	-	-	-	-	09.5	0.05	e
232	11 12 05.6	-61 18 34.3	-	-	-	-	-	-	08.8	0.06	e
233	11 12 06.6	-61 19 28.5	-	-	-	-	-	-	10.2	0.06	e
234	11 12 08.1	-61 19 26.8	-	-	-	-	-	-	09.7	0.06	e
235	11 12 10.9	-61 18 54.3	-	-	-	-	-	-	09.1	0.06	e
236	11 12 13.4	-61 17 58.5	-	-	-	-	-	-	10.0	0.06	e
237	11 12 14.0	-61 15 29.4	-	-	-	-	-	-	10.6	0.10	e
238	11 12 16.1	-61 16 11.4	-	-	-	-	-	-	09.8	0.06	e
239	11 12 16.8	-61 16 16.2	-	-	-	-	-	-	10.5	0.08	e
240	11 12 18.0	-61 15 42.7	-	-	-	-	-	-	10.7	0.10	e
241	11 12 18.2	-61 20 58.2	-	-	-	-	-	-	10.4	0.05	e
242	11 12 22.0	-61 20 52.5	-	-	-	-	-	-	11.1	0.07	e
243	11 12 26.6	-61 20 17.7	-	-	-	-	-	-	10.6	0.04	e
244	11 12 28.5	-61 22 21.2	-	-	-	-	-	-	09.6	0.03	e
245	11 12 29.4	-61 19 55.6	-	-	-	-	-	-	11.0	0.05	e
246	11 12 29.7	-61 20 27.9	-	-	-	-	-	-	10.8	0.06	e
247	11 12 30.0	-61 21 29.7	-	-	-	-	-	-	09.7	0.04	e
248	11 12 30.8	-61 21 19.8	-	-	-	-	-	-	10.3	0.04	e
249	11 12 32.9	-61 20 14.7	-	-	-	-	-	-	10.9	0.04	e
250	11 12 41.6	-61 16 06.0	-	-	-	-	-	-	11.1	0.05	e
251	11 12 55.4	-61 16 43.5	-	-	-	-	-	-	09.6	0.24	e